

Finite element modelling of transport in a tokamak edge and divertor.

Richard Marchand

Department of Physics, University of Alberta, Edmonton Alberta, T6G 2J1 Canada

Abstract

A finite element approach is described, for modelling transport in tokamak edge and divertor plasma. The method discretizes all transport equations on an unstructured triangular mesh. The advantages and difficulties of this approach are discussed. Results are presented and compared with experimental measurements made on TdeV. Example results are also given for JET, using a simplified physics model (single ion species, no neutrals and no flux limits), and using a more comprehensive model with helium impurity ions and neutrals.

1. Introduction

This letter presents a different approach to modelling the edge and divertor regions of tokamak plasmas from the ones generally in use. Plasma transport in tokamaks is almost universally modelled with a finite volume discretization on structured quadrilateral meshes[1-4]. While this method is well established and broadly adopted, it has some notable drawbacks and limitations. In particular, it does not lend itself naturally to an arbitrary SOL topology, it is limited in the ways in which the mesh may be refined, and the quadrilateral cells sometimes need to be highly stretched and twisted to accommodate divertor plates that are nearly tangent to the magnetic field lines. To be fair, this approach also has some strengths; the main ones being its relative simplicity, and its natural ability to accurately represent strong transport anisotropies in a magnetized plasma. In the following, the transport model and the discretization scheme are briefly described. Example simulations are then given for a pure deuterium plasma, and comparisons are presented with measurements made in the now decommissioned TdeV experiment. These comparisons focus on the H-alpha emissivity, the ion temperatures in the divertor and on the pumping efficiency of helium. Sample results are also presented for JET, for an idealized pure deuterium plasma, and for plasmas with a small concentration of helium.

2. Model description

A detailed description of the physical model and the numerical method used to solve the transport equations can be found in [5]. It is briefly summarized here for completeness. Transport of charged species is described in the fluid approximation. The equations for the conservation of particles, parallel momentum and energy are solved for every (positively charged) ionisation stage in the plasma. In addition, an equation is also solved for the conservation of electron thermal energy. Neutral particles transport is described in the diffusion approximation; that is, equations are solved for the conservation of neutral particles density and energy. In all cases, fluxes of neutral particles and energy are assumed to be purely diffusive, with a diffusion coefficient depending on the local collision and charge exchange mean free paths. Unless stated otherwise, all fluxes parallel to the magnetic field are classical, with a flux limit of 0.2. Uniform perpendicular diffusion coefficients are used to account for anomalous transport in the perpendicular direction. Boundary conditions are specified for the charged species densities and temperatures at the boundary between the SOL and the central region. At the divertor plates, the parallel velocity is

assumed to be equal to the local sound speed. Standard sheath boundary conditions are assumed for the electron and ion thermal fluxes at the plates. The parallel electron thermal energy flux there is taken to be $Q_{\parallel e} = \delta_e n_e T_e C_s$, where C_s is the sound speed, and $\delta_e = 5$. A similar expression is used for the ion thermal energy flux at the plate, with $\delta_i = 2.5$. Finally, the effect of $\mathbf{E} \times \mathbf{B}$ drifts is always ignored. In practice, the inclusion of drift effects is found to have a large effect on the parallel velocity [5]. The other plasma profiles and net poloidal flows, however, are found to be relatively insensitive to the inclusion of drifts. The result is a set of several coupled nonlinear partial differential equations for the unknown variables. These are discretized with finite elements, using linear interpolation functions on an unstructured triangular mesh.

The development of this finite element approach was motivated by the following facts:

- 1) An unstructured mesh does not involve any artificial cut at the X point(s) as required when mapping a structured mesh onto a SOL. Once the model is developed for a given geometry, it is a straightforward exercise to extend it to other magnetic configurations with one or two X points, and boundaries (divertor plates) of arbitrary shapes. This applies to divertor, limiter or mixed configurations.
- 2) The problem associated with stretching and distortion of quadrilateral cells in the vicinity of divertor plates is notorious. This problem is absent with an unstructured grid. As a result, the construction of a suitable unstructured mesh is generally less problematic than that of a structured one. A difficulty with the use of general distorted quadrilateral meshes is the necessity to use a finite discretisation for the diffusion operator with a minimum of nine points. When the mesh is not orthogonal, the requirement of having a difference operator that is conform to the initial differential operator, and that of having a positive definite difference operator (needed to ensure positive mass and energy) are known to be incompatible [6]. Indeed, Kershaw illustrated how skewness in the mesh could induce distortions in the solution of a transient diffusion problem. The assessment of distortions appearing in a convective-diffusion problem such as that of particle and heat transport near divertor plates in a tokamak would require a detailed comparisons between codes, which is beyond the scope of the present article.
- 3) Finally, a triangular unstructured mesh offers more flexibility for spatial refinement.

Figures 1 and 2 give examples of a structured and unstructured meshes calculated in the divertor region of JET. The issue of mesh refinement and spatial resolution is particularly obvious in the vicinity of the X point in both cases. For the structured mesh, the construction of a quasi-orthogonal mesh results in rather large cells at the X point being linked to (unnecessarily) small cells radially outward. In this case, increasing the resolution at the X point would imply even smaller cells away from it, where a finer resolution may not be needed. From Fig. 2, it is clear that mesh points may be added near the X point, and not affect the distribution of mesh points elsewhere. It should be noted that, in a finite element discretisation, unknowns are defined at node points while, in a finite volume discretisation, some are defined at cell centres and some at cell interfaces. Therefore, while the number of triangles in an unstructured mesh is larger than the number of quadrilateral cells used in a structured mesh, the total number of unknowns is comparable. In the particular case illustrated in Fig. 2, the unstructured mesh was constructed

from a typical structured mesh used to model transport in JET. Several nodes have been eliminated in the triangular mesh, which would have appeared in the structured mesh, and some points were added near the X point. The total number of nodes (1489) is comparable to the number of cells (1800, not counting ghost cells at the boundaries) that would typically occur in structured mesh of the type used in the B2 code.

To be fair, a discretization based on an unstructured mesh comes with its own difficulties. Perhaps the most serious one is related to the necessity for strict alignment along the magnetic flux surfaces. This is required in order to preserve the strong anisotropy in electron thermal transport. It can indeed be demonstrated that, in order to avoid numerically corrupting the (weak) anomalous perpendicular transport by the (much stronger) parallel transport, most cells must have a side that is parallel to the local magnetic field. In practice, this is achieved by requiring that the extremities of the aligned side be on the same magnetic flux surface. This actually imposes a serious constraint on the construction of unstructured meshes which, in their poloidal distribution, must be very similar to structured meshes. Alignment alone is, however, not sufficient to prevent corruption of perpendicular thermal diffusion by parallel transport. This can be understood by considering the following diffusive equation in which a diffusive flux only exists in the parallel direction, defined by the unit vector field \mathbf{b} :

$$\frac{\partial T}{\partial t} - \nabla \cdot (\hat{\mathbf{b}} \hat{\mathbf{b}} \mathbf{k} \cdot \nabla T) = 0. \quad (1)$$

If the unknown field is expressed as a superposition of linear interpolating functions N_j and if the resulting equation is multiplied by N_i and integrated over the entire domain, then, the second term in (1) yields, after an integration by parts,

$$\int d^2x \kappa (\nabla N_i \cdot \hat{\mathbf{b}}) (\nabla N_j \cdot \hat{\mathbf{b}}) \quad (2)$$

where the integration is carried over an element (a triangle). In order to ensure that this discretization does not lead to spurious transport in the perpendicular direction, it is necessary to ensure that the integral in (2) vanishes whenever nodes i and j are not on the same flux surface. Thus, referring to Fig. 3, it follows that the integral in (2) should vanish because i and j are on different field lines. For a curved field, and for finite size elements, this integral (and its numerical estimation) does not vanish exactly in general. The result is a spurious transport in the direction perpendicular to the field \mathbf{b} . In the case of electron thermal diffusion, where the parallel diffusivity exceeds the (anomalous) perpendicular diffusivity by many orders of magnitude, even a small non-vanishing contribution from this integral leads to a non acceptable corruption of perpendicular diffusion. For that reason, it is necessary to take some special action in assembling the global matrix (where integrals such as (2) are used) of the finite element formulation, to make sure that parallel thermal diffusion only couples nodes that are on the same field lines.

3. Results

In this section, simulation results are presented for representative TdeV operational conditions. Comparisons between simulation predictions and experimental measurements are made for the ion temperatures, for H-alpha emissivity and for helium enrichment in the pumping plenum. Results

are also presented for JET; first with a very simple and idealized physics model, then with a more complete model.

3.1 D-alpha emissivity and ion temperatures in TdeV 95.

We first present some results obtained with the original TdeV divertor geometry, referred to here as TdeV 95. The upper divertor region of that geometry is illustrated in Fig. 4, for reference. In these simulations and in the ones presented in the next section, the particle anomalous perpendicular diffusivity and the perpendicular viscosity (in the parallel momentum equation) are taken to be $0.4 \text{ m}^2\text{s}^{-1}$. The electron and ion anomalous thermal diffusivities are $1.2 \text{ m}^2\text{s}^{-1}$. The results were obtained for discharge conditions corresponding to an intermediate density (line average density of approximately $4 \times 10^{19} \text{ m}^{-3}$), at which partial detachment is observed. These conditions are close to those of an experiment analysed recently by Meo, et al. [7]. In this simulation, carbon impurities are taken into account. A small fraction (1%) of CV was assumed at the boundary with the central plasma. Carbon sputtering by DII is taken into account, with a fixed yield of 2%. Sputtering by other species (charged or neutral) is ignored. A 100% recycling coefficient is assumed for deuterium. All carbon fluxes incident on the plates are assumed to be totally absorbed. Figure 5 shows the D-alpha emissivity calculated in the outer divertor as a function of the height Z above the midplane. As in Ref. 5, for each height Z above the midplane, the emissivity is scanned horizontally to determine the maximum value, and only this value is plotted as a function of Z. The dashed lines in Fig. 4 shows the trajectories along which the maximum emissivities are plotted. It would not be meaningful to attempt a precise quantitative comparison between these results and those of Ref. [7], because the equilibria considered are different. Indeed, the simulations results presented here were obtained for shot 26565 at 250 ms, while Meo, et al., report time integrated D-alpha emissivities for shots 26281 and 26574. It is nonetheless interesting to note that the calculated D-alpha emissivity is of a comparable magnitude as the inferred experimentally. There are also some interesting differences. In particular, in the fact that the calculated emissivity decreases to nearly zero at the upper divertor plate ($Z=0.44\text{m}$). This feature of the simulated emissivity is independent of the exact equilibrium or of the precise position of the strike point with the upper divertor plate. The D-alpha emissivity calculated from the finite element simulation is always found to decrease near the plates. The larger values determined experimentally may be associated with molecular dissociation processes, not included in the model.

Another calculation of interest is the ion temperatures for DII and the first four ionisation stages of carbon. This provides a direct test of the “single ion temperature” approximation made in most other tokamak edge and divertor transport models. The ion temperatures, determined along the same trajectory as the D-alpha emissivity presented above, are plotted in Fig. 6. For reference, the electron temperature is also plotted along the same trajectory. The important thing to note is that not all ion species have the same temperature. Indeed, CII has a significantly lower temperature close to the divertor plate, where it is generated from the ionisation of ‘cold’ carbon neutrals, and where charge-exchange cooling is significant. The temperatures of the higher ionisation stages are larger, and closer to that of DII, with CIV being the closest. This faster equilibration of the higher

ionisation stages with DII is an obvious consequence of the strong increase of the collision frequency with ion charges. We conclude from these results that, for practical purposes, the single ion temperature approximation is acceptable for higher ionisation stages of impurity ions. Lower ionisation stages of impurity ions, however, cannot be modelled with the same temperature as the bulk ions. At least close to the divertor plates (where their density is significant), they require to be described with their own temperature or, possibly, with kinetic theory.

3.2 Helium enrichment in TdeV 96.

Helium enrichment η in the pumping plenum of TdeV has been determined experimentally for two configurations [8] in the final divertor geometry of TdeV. In one, the entrance to the pumping plenum is through the private region (Inboard Pumping) while, in the other (Fig. 7), it is through the SOL (Outboard pumping). Experimentally, He enrichment was defined as the ratio of helium to deuterium neutral density in the pumping plenum, divided by the ratio of helium to deuterium ion densities in the central plasma. In the simulations, enrichment is defined as the ratio of neutral helium flux to the deuterium flux at the entrance of the pumping plenum, divided by the ratio of the helium density to the deuterium density at the boundary between the SOL and the core region. These two definitions are not rigorously equivalent. They should be approximately equivalent if 1) the ratio of He to D is approximately uniform throughout the core plasma, and 2) if the ratio between the particle flux into the pumping plenum is the same for both species.

Referring to Fig. 2 of [8], the outboard pumping configuration considered here corresponds to the middle configuration, while the inboard configuration corresponds to the one on the right. A comparison between simulated and measured enrichments is given in Fig. 8. The enrichment calculated from B2-EIRENE simulations is also plotted for comparison. In relating experimental and simulation results, use is made of the fact that the ratio between the average linear density $\langle n_e \rangle$ and the density at the separatrix typically range between 5 and 6 [9]. Thus, a fixed ratio of 5.5 is assumed. The enrichment factor calculated from the finite element simulations is seen to be systematically larger than the ones reported from the experiment, by a factor of approximately 2. The values of η determined experimentally, on the other hand, are larger than the ones determined from B2-EIRENE by a factor ranging between 1 and 2, with the better agreement occurring at the higher densities. Quantitatively, the differences between simulation and experiment may be attributed to the differences in the definitions of η , or to the assumption made for the ratio between the averaged density and the density at the separatrix. The differences between the two simulations are mostly attributable to the numerical and physical models themselves. In particular, the neutral transport model used in B2-EIRENE accounted for the detailed geometry and material properties in the TdeV vacuum chamber. It also includes an extensive set of molecular and atomic processes. The neutral transport model used in the finite element simulation is based on a simple diffusion approximation. It accounts for a number of atomic processes (ionisation, recombination, radiative cooling and losses), but it does not account for the presence of molecules near the divertor plates. In all cases, enrichment is seen to be a decreasing function of the average density at lower densities and, for experimental and finite element results, η decreases less rapidly as a function of density at higher densities. From B2-EIRENE, η becomes an increasing function of density for the larger densities. An interesting

qualitative difference between the experiment and either simulation results is the crossover in η at $\langle n_e \rangle \sim 6 \times 10^{14} \text{m}^{-3}$. At low densities, the experimental enrichment is highest for inboard pumping while for the larger densities, it is larger for outboard pumping. This is not reproduced in either simulation. Another difference, between the models, is that B2-EIRENE predicts a larger enrichment for inboard pumping, over the entire density range considered, while the finite element simulations predict the opposite. The difference between the two values of η calculated with B2-EIRENE is nearly independent of density. This difference, when η is calculated with the finite element model, increases markedly at larger densities, which agrees qualitatively with experiment.

3.3 Example simulation with JET: simplified physics model.

Simulations have been made for the JET geometry with a greatly simplified physics model. In these, particle recycling and the presence of neutral species are ignored, and all flux limits are turned off. The purpose of these simulations is to facilitate an eventual comparison with other numerical approaches by presenting results that will depend more on the specific numerical methods, rather than on the particular physics model. The mesh used in the simulations is illustrated in Fig. 2, in the vicinity of the divertor region. The innermost flux surface in the midplane ($z=0.393\text{m}$) extends to $R=3.824\text{m}$. In that plane, the separatrix extends to $R=3.858$ and the outermost flux surface extends to $R=3.890$. The density assumed at the boundary with the central region is 10^{19}m^{-3} , and the temperature there is 200eV . The anomalous transport coefficients are $1 \text{m}^2\text{s}^{-1}$ for perpendicular particle transport and for perpendicular viscosity, and $2 \text{m}^2\text{s}^{-1}$ for perpendicular energy transport. This, at steady state, yields an input power of approximately 1.2MW from the core to the SOL. Of that, 60% is calculated to be deposited on the outer divertor plate, and 40% on the inner plate. The resulting electron density profile is shown in Fig. 9. It is, of course, not possible to compare the results obtained in this approximation with experimental measurements. They are presented to illustrate the type of comparison that would be possible with other calculations.

An interesting feature to note in Fig 9 is the local maximum in density in the vicinity of the X point. This feature is associated with the plasma flow towards the divertor plates and with anomalous perpendicular viscosity in the momentum equation. The result is a flow toward the X point just inside the separatrix. This converging flow is responsible for the gentle accumulation of plasma at the X point, just inside the separatrix. It should be noted that this feature is only manifest if the mesh resolution near the X point is high enough. In particular, in simulations made with structured quadrilateral meshes, the spatial resolution is typically poor near the X point, and this feature would not be visible. The appearance of a local density maximum near the X point is obviously not related to the formation of a MARFE because of the neglect of recycling in this simulation. Under more realistic conditions, however, it is plausible that a seed density maximum near the X point, associated with plasma flow convergence there, would influence the evolution of a MARFE.

3.4 Example simulation with JET: more representative plasma conditions.

Figures 10 and 11 illustrate some simulation results obtained with the more complete physics

model described in Sec. 2. The conditions imposed for the deuterium density and temperature at the boundary with the central plasma are the same as in 3.3. The main difference here is that flux limiters with $f=0.2$ are used in all (otherwise classical) parallel fluxes. At the boundary with the centre, a fixed density ratio of 10% is assumed between helium and deuterium; that is, the helium density is assumed to be 10^{18}m^{-3} there. The helium temperature at that boundary is assumed to be 200eV, as for the other species. Plasma sputtering at the divertor plates is neglected, but both deuterium and helium are assumed to recycle with 100% efficiency. A comparison of Figs. 9 with 8 shows the effect of the simplifications made in 3.2. The effect of recycling as a source of plasma is obvious from this comparison. The plasma density calculated in the divertor is significantly larger, and the profile is qualitatively different when recycling and neutral ionisation are taken into account. Finally, Fig. 11 shows the calculated two dimensional distribution of neutral helium density. This figure indicates that the highest concentration of HeI is on the divertor plates, very close to the strike point with the separatrix.

4. Summary and conclusion

In summary, a comprehensive two-dimensional model has been developed to simulate transport in tokamak edge and divertor regions. This model uses a numerical approach that is different from the one used generally in other models. This alternative approach has the advantage of allowing more flexibility in defining the spatial mesh resolution. Because it uses a triangular unstructured grid, it is free of the problems associated with stretched and distorted cells at divertor boundaries, when the magnetic field is nearly tangent to the plates. It is also readily applicable to a broader class of magnetic field configurations including divertor, limiter, or mixed configurations. Results have been obtained that are in reasonable agreement with measurements made on TdeV. An interesting feature of the model is that it allows for as many ion temperatures as there are ion species. Simulations made for TdeV indicate that the single ion temperature approximation, used in other transport models, is indeed a good approximation for all charged species, except for the lower impurity ionisation stage(s). In the divertor region and generally, in regions with strong recycling, these species are affected by a strong ionisation source of cold ions and by charge exchange with 'cold' neutrals. As a result, their temperature is significantly lower than that of the bulk ions. A proper description of these species thus requires, at least, a separate ion energy equation. In instances when very different ion temperatures, or temperatures with strong parallel gradients would be predicted, a kinetic description of the ion species may even be required.

Acknowledgement

Thanks to Alberto Loarte and Andrei Kukushkin for kindly providing JET equilibria and structure files. I am grateful to J.-L. Gauvreau for some e-mail exchanges concerning helium enrichment measurements in TdeV. This work made use of the Multimedia Advanced Computational Infrastructure (MACI) supported jointly by the Canada Foundation for Innovation and by the Alberta Innovation and Science Research Investment Program. This work was supported by the Natural Sciences and Engineering Council of Canada.

References

1. R. Schneider, et al., J. Nucl. Mater. 220-222, 1076 (1995).
2. S. Tsuji, et al., J. Nucl. Mater. 220-222, 400 (1995).
3. A. Taroni, et al., J. Nucl. Mater. 220-222, 1086 (1995).
4. G.R. Smith, et al., J. Nucl. Mater. 220-222, 1024 (1995).
5. R. Marchand and M. Simard, Nucl. Fusion 37, 1629 (1997).
6. D. Kershaw, J. Comp. Phys. 39, 377 (1981).
7. F. Meo, et al., Phys. Plasmas 7, 2494 (2000).
8. J.-L. Gauvreau, et al., J. Nucl. Mat 266-269, 307 (1999).
9. J.-L. Gauvreau, private communication

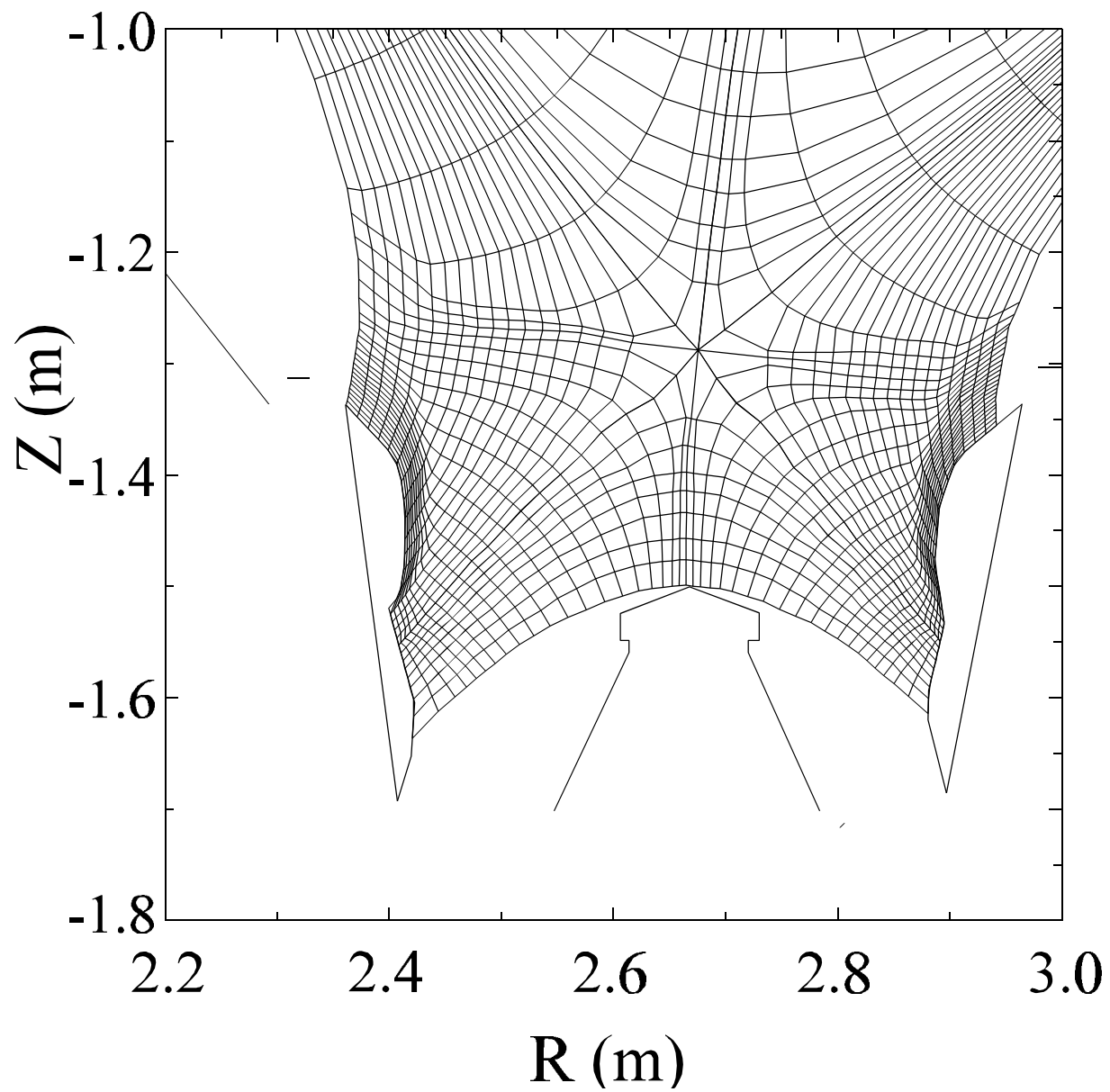


Fig. 1. Illustration of a structured quadrilateral mesh computed for JET, in the divertor region.

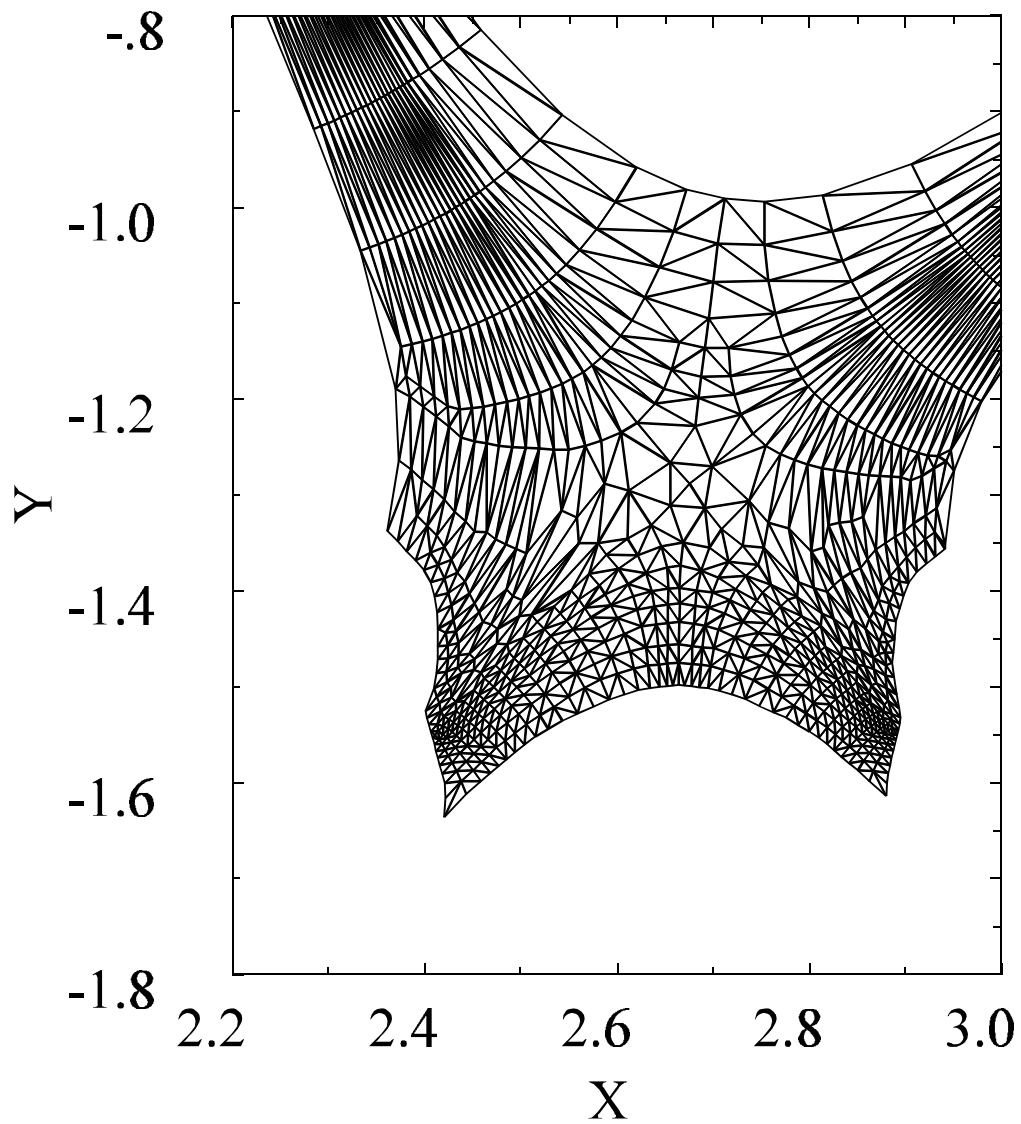


Fig. 2. Illustration of a triangular unstructured mesh computed for JET, in the divertor region.

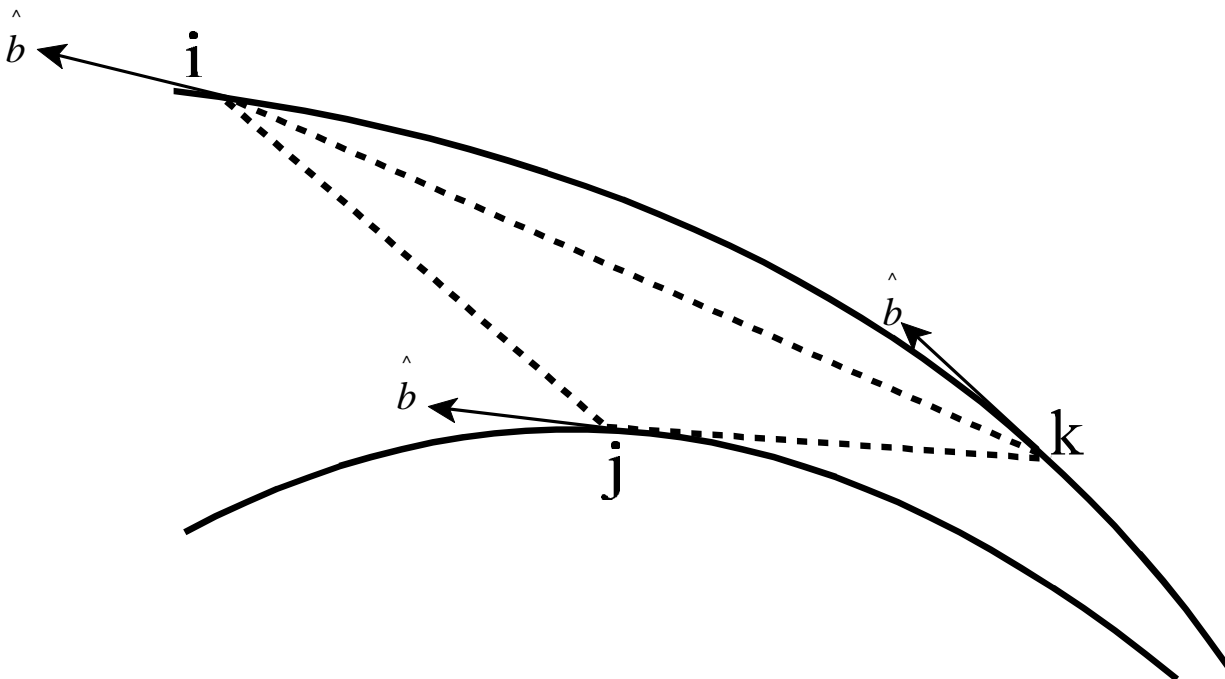


Fig. 3. Illustration of an 'aligned' triangular element in the presence of curved magnetic surfaces.

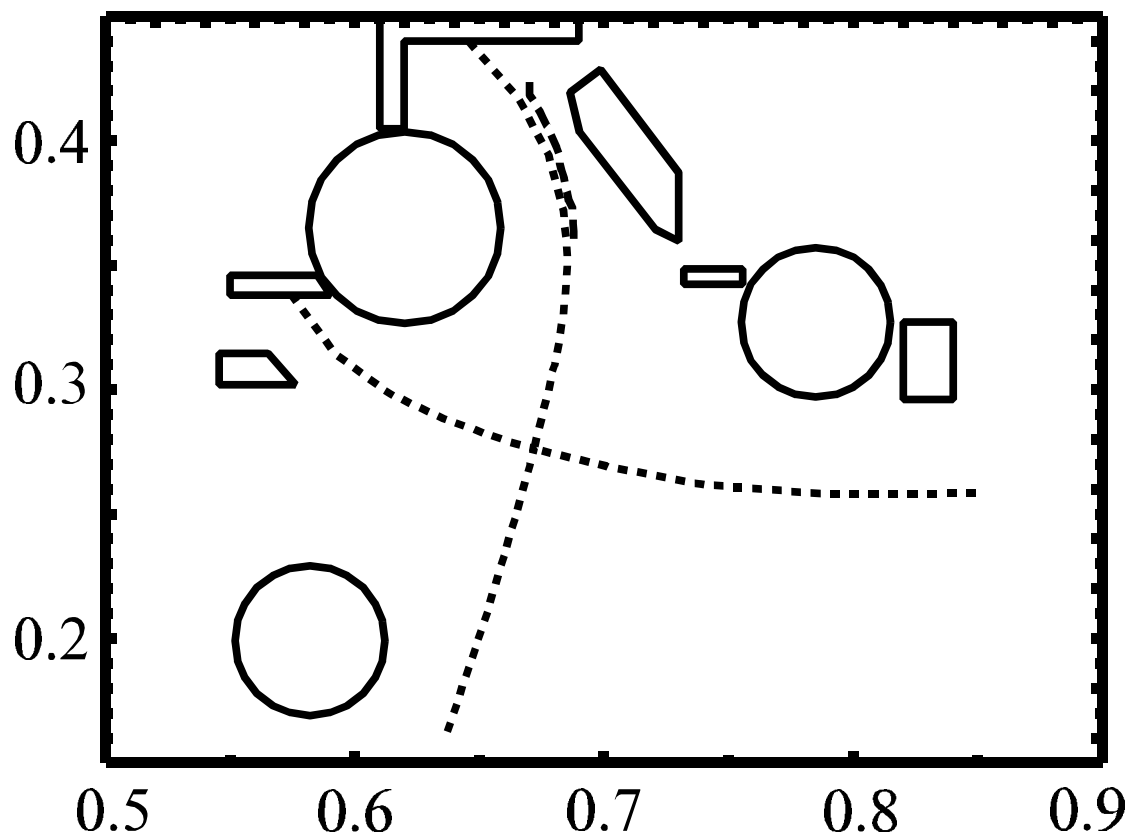


Fig. 4. Illustration of the divertor region in TdeV95. The dotted lines show the separatrix for the equilibrium considered. The dashed line (near the separatrix) shows the trajectory along which the D-alpha emissivity is plotted in Fig. 5.

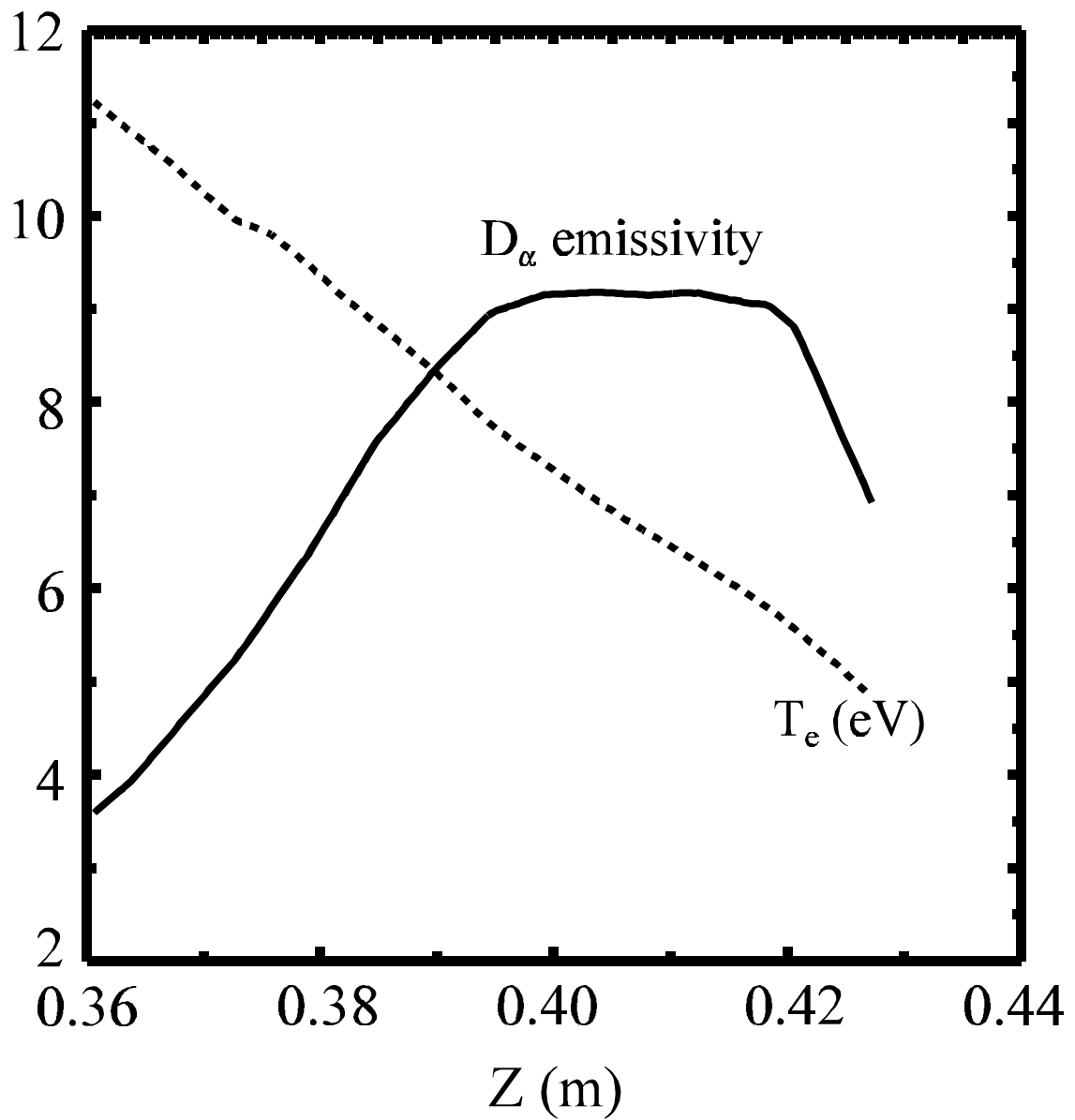


Fig. 5. Maximum D-alpha emissivity as a function of the vertical position above the midplane Z . For each Z , the emissivity is scanned horizontally in the outer divertor to determine the maximum value. The emissivity is in units of 10^{21} photons radiated per second, per cubic metre. For reference, the divertor plate is located at $Z=0.44$.

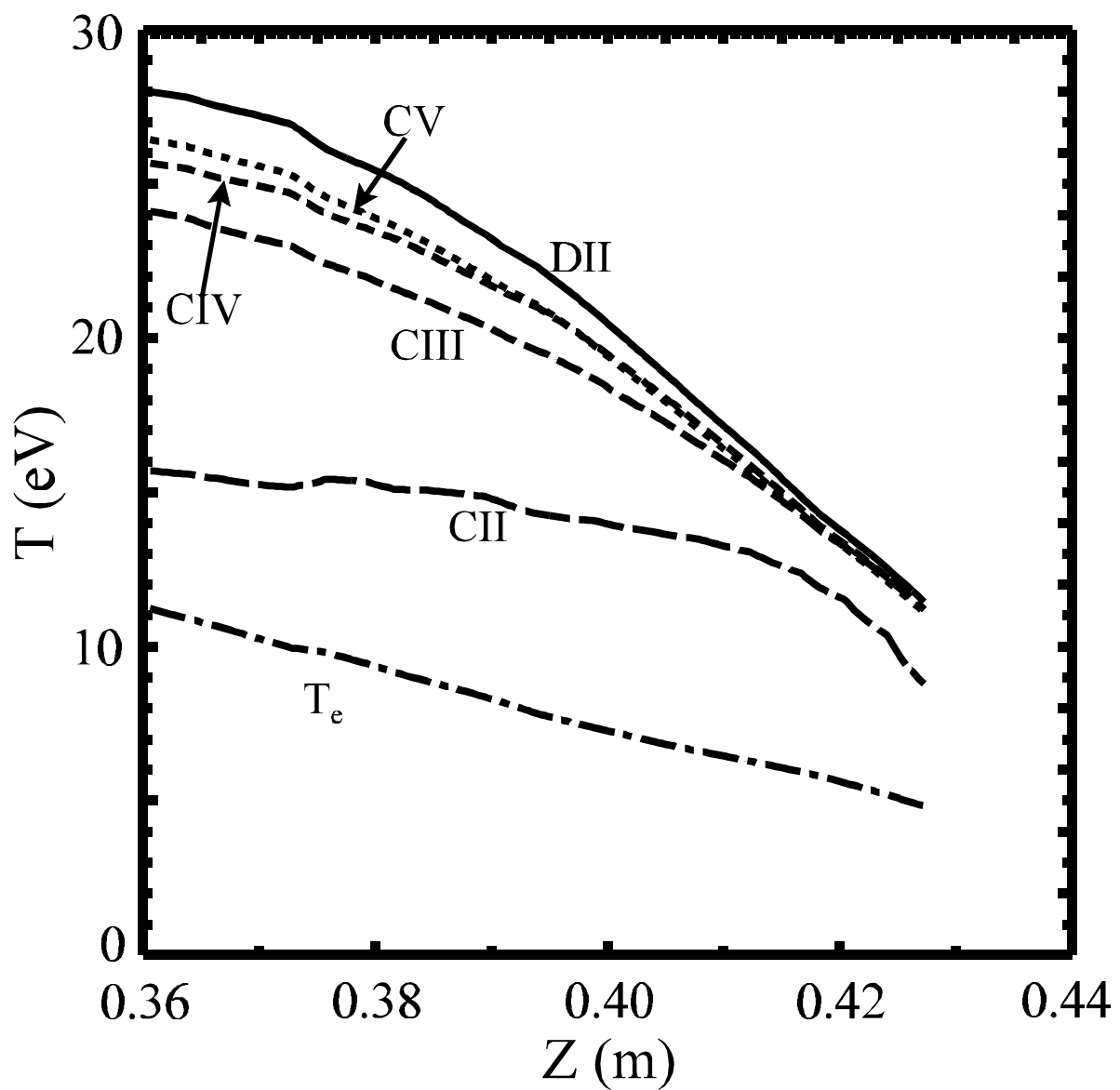


Fig. 6. Electron and ion temperature profiles calculated for DII, CII, CIII, CIV and CV between the X point and the divertor plate, along the line of maximum horizontal D_α emissivity, as in Fig. 5. For reference, the divertor plate is located at $Z=0.44$.

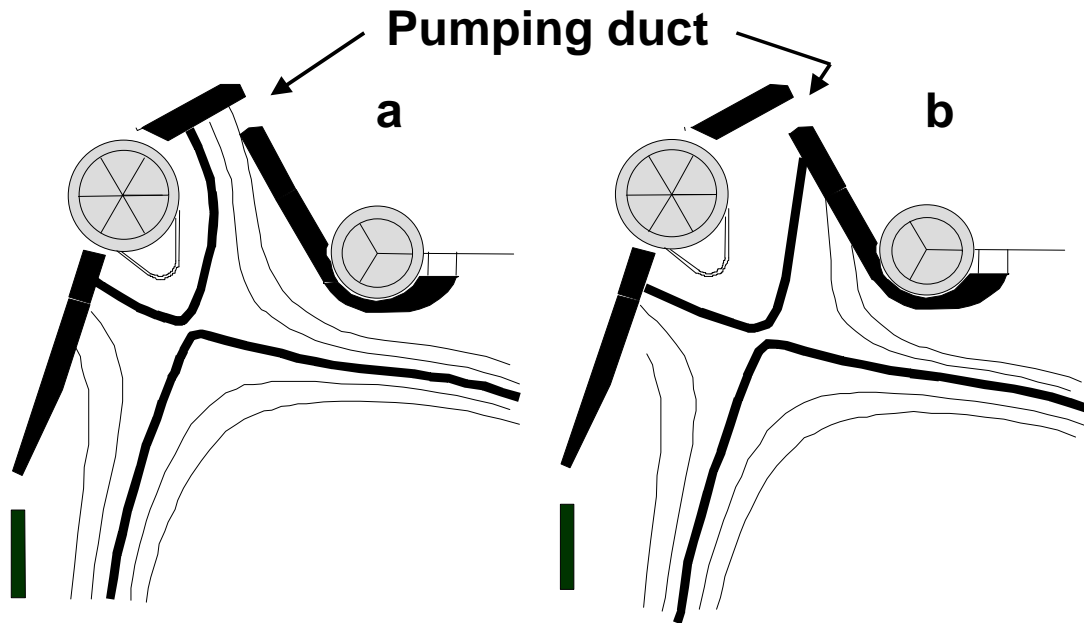


Fig. 7. Illustration of the pumping configuration in TdeV. In the outboard configuration (a), the separatrix intersects the upper divertor plate and the entrance to the pumping plenum is through the SOL. In the inboard pumping configuration (b), the separatrix intersects the lower (oblique) divertor plate. In that case, entrance to the pumping plenum is through the private region.

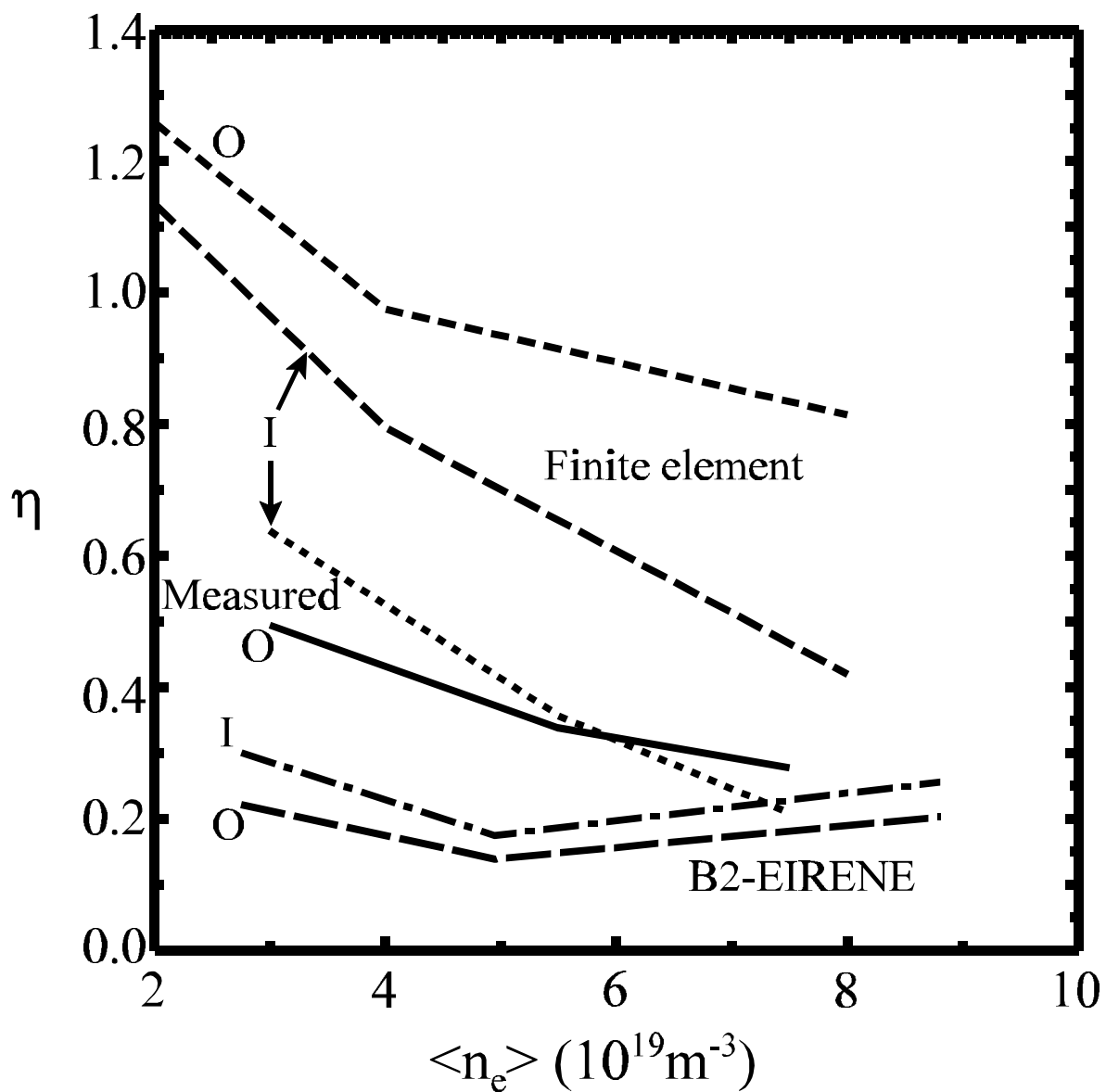


Fig. 8. Comparison between the measured and simulated helium enrichment at the entrance of the pumping plenum in TdeV, for inboard (I) pumping and outboard (O) pumping.

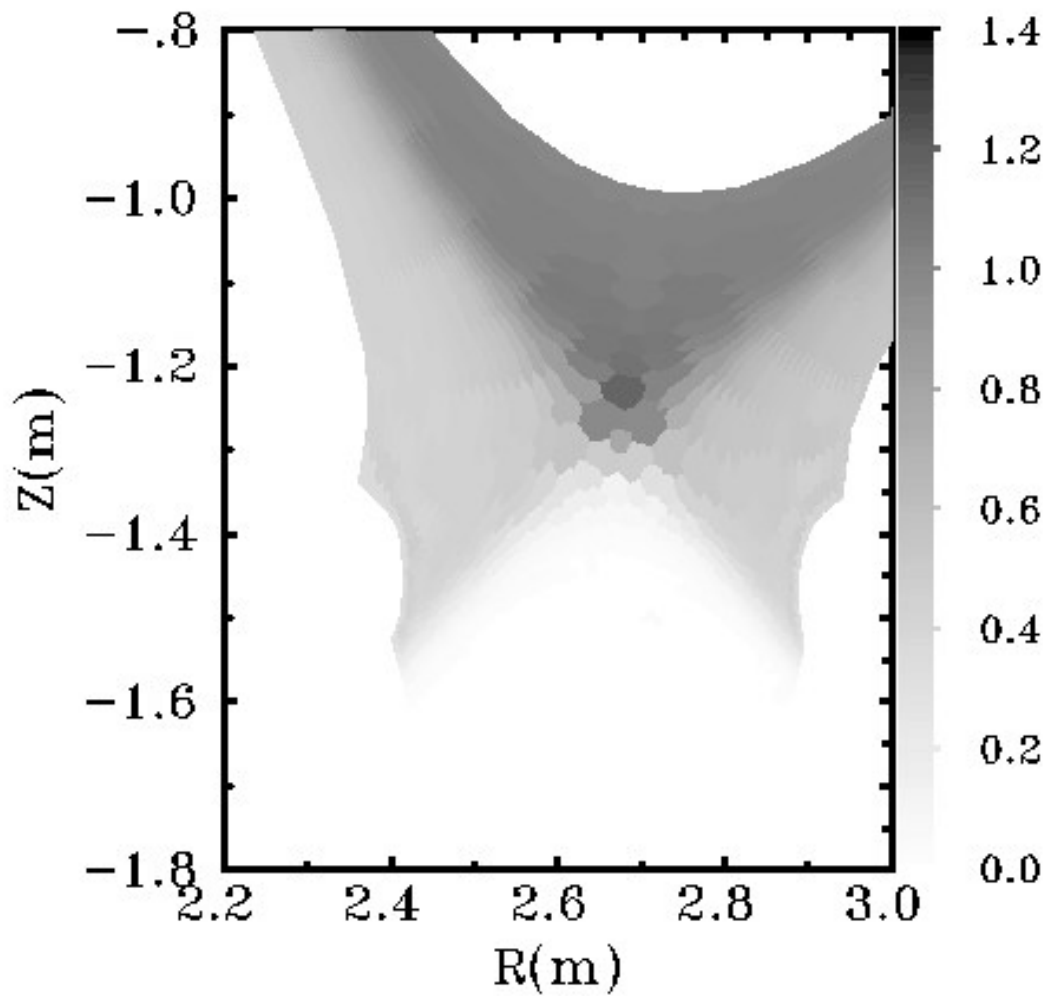


Fig. 9. Two dimensional electron density profile computed for JET with the reduced physics model. The density is in units of 10^{19}m^{-3} .

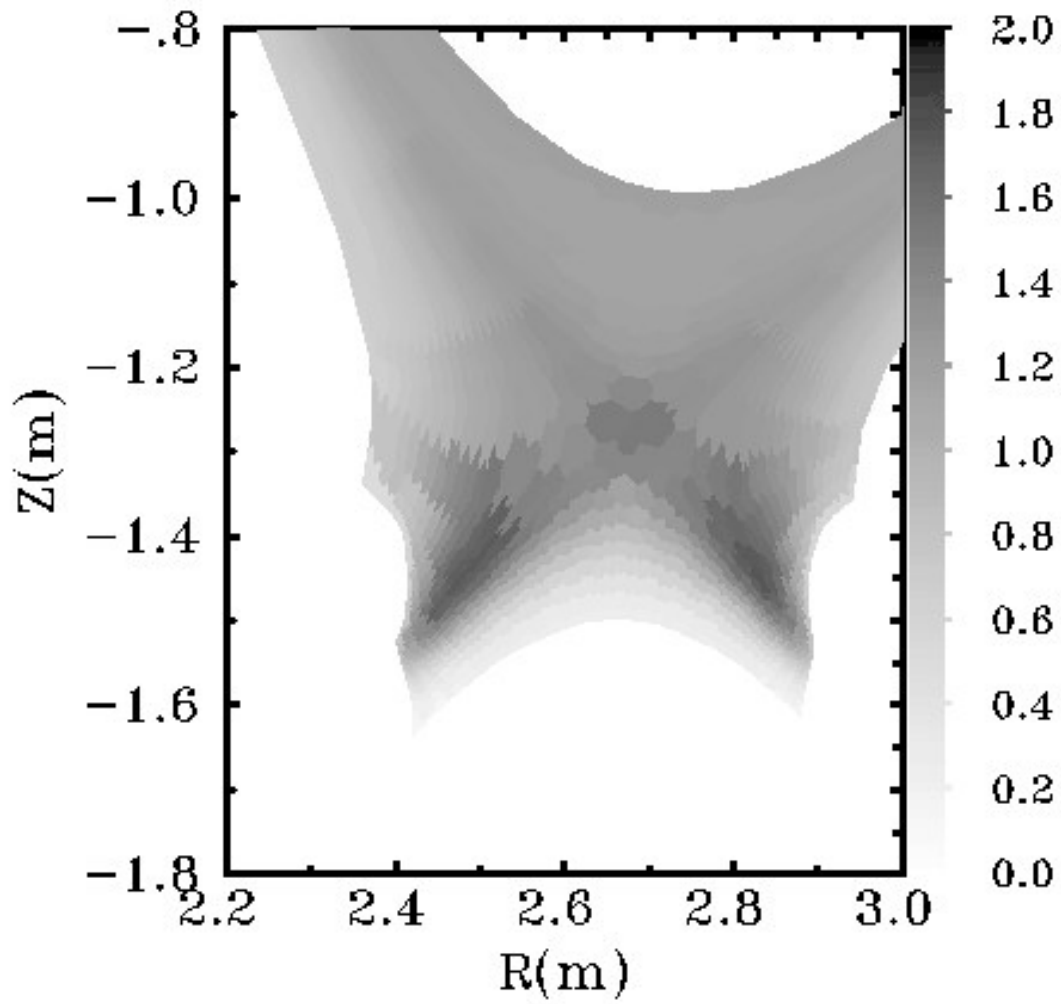


Fig. 10. Two dimensional electron density profile computed for JET with the more complete physics model. The density is in units of 10^{19}m^{-3} .

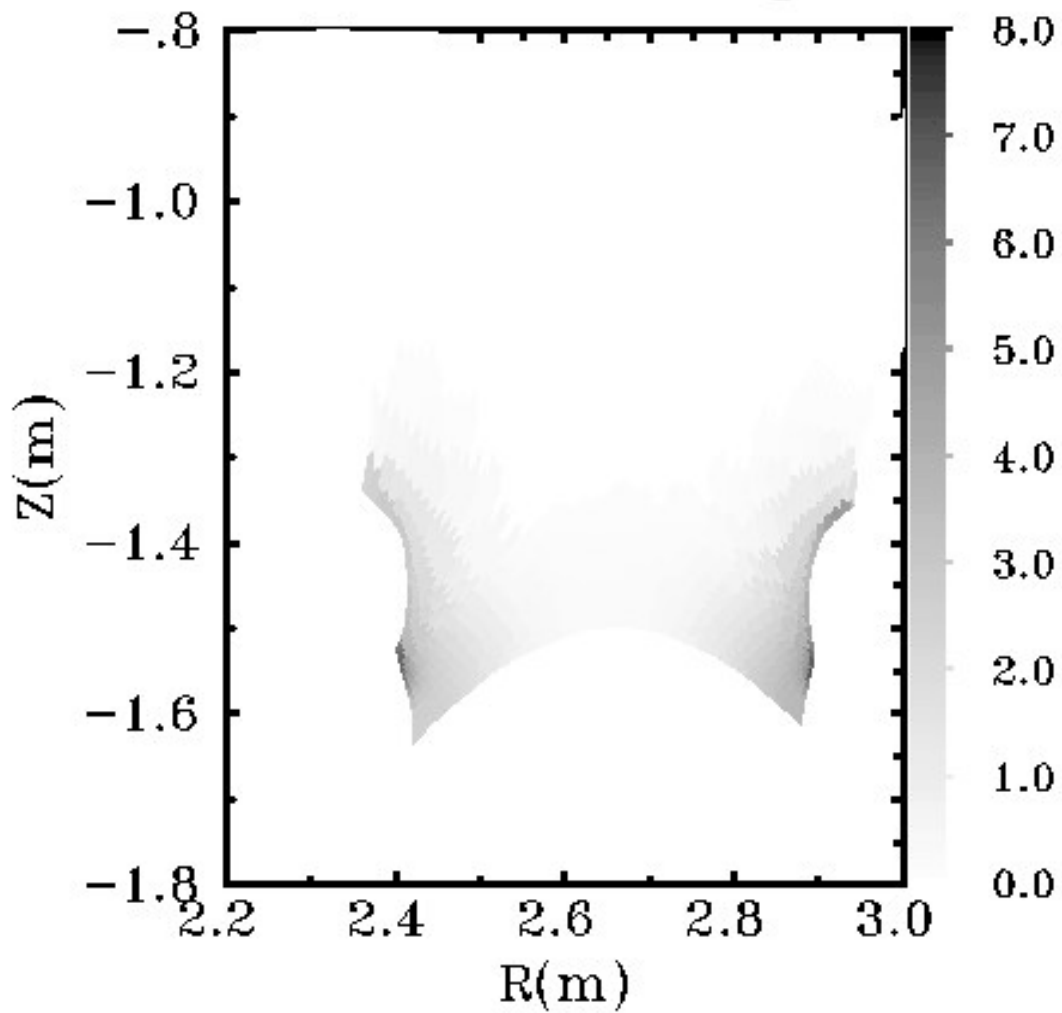


Fig. 11. Two dimensional neutral helium density profile computed for JET with the more complete physics model. The density is in units of 10^{17}m^{-3} .